Computational Aerothermodynamics for HTV Small Re-entry Capsule Project

Keiichiro FUJIMOTO*, Takayuki ITOH**, Hideyo NEGISHI, Ryoh NAKAMURA, Yasuhide WATANABE, Kota TANABE*

*Japan Aerospace Exploration Agency

JAXA, 2-1-1, Sengen, Tsukuba, Ibaraki, Japan

fujimoto.keiichiro@jaxa.jp , negishi.hideyo@jaxa.jp , nakamura.ryoh@jaxa.jp

watanabe.yasuhide@jaxa.jp , tanabe.kota@jaxa.jp

**East Japan Institute of Technology Co., Ltd

itoh.takayuki@jaxa.jp

Abstract

Successful result of HTV small re-entry capsule (HSRC) project was presented. Computational aerothermodynamic analysis methods and its contributions to the HSRC's design are overviewed and discussed. Local heat flux peak and the pressure increase are generated due to the hot gas main stream collision onto the wall near the reaction control system (RCS) nozzle exit. Augmentation factor is roughly from 2.0 to 8.0, which is increased by the larger mass flow rate of the free-stream. Effect on the aerodynamic force and moment is significant, which is at least 5 times larger as comparing with the RCS thrust. Severe ablator erosion was not found and the precise GNC was achieved. TPS shell separation failure and collision risks were identified and the shell release air-bag was employed. Its importance on the reliable parachute deployment is confirmed by the post-flight analysis. Conventional MILES-type computational fluid dynamics (CFD) analysis is quantitatively accurate even for the unsteady flows such as the aeroacoustic characteristics prediction. Pressure fluctuation is induced by the unsteady shear layer whose frequency changes with the flow structures such as the local shock on the shear layer. Input sound pressure level is decided based on CFD. 6DoF trajectory analysis was carried out to evaluate the side-wind criterion to prevent the turn-over rotation at the low dynamic pressure phase just after the separation. Drop test was succeeded by meeting the side-wind criterion.

1. Introduction

Re-entry return-to-Earth technology is key element to establish a reliable and affordable access to space, so that comprehensive research and development efforts have been made in all over the world. In the last twenty years, the comprehensive research and development activities have been carried out also in Japan to establish reliable return-to-Earth system. The orbital re-entry experiment (OREX) and hypersonic flight experiment (HYFLEX) were successfully completed in 1994 and 1996 respectively, those were preparative flight experiments for the H-II Orbiting Plane (HOPE) [1]. In Muses-C sample return mission from the near-Earth asteroid "Itokawa", the re-entry capsule and the spacecraft re-entered atmosphere at the extremely severe heating conditions and samples

Figure 1: Mission sequence overview for HSRC.

were successfully delivered to the Earth in 2010 [2]. Those projects were successfully completed, and important flight data had been acquired. Consequently, the technology readiness level of the design, manufacturing and operation were significantly improved and validated through successful returns from the space. The small re-entry capsule vehicle installed on H-II transfer vehicle (HTV), named HTV small re-entry capsule (HSRC) has been developed at Japan Aerospace Exploration Agency (JAXA), in order to demonstrate return-to-Earth system to deliver the experimental samples from the international space station (ISS) [3]. Schematics overview of its mission sequence is shown in Figure 1. After the cargo delivery to the international space stations (ISS), HTV is disposed by the destructive atmospheric re-entry in the current operation. At the re-entry initial phase, re-entry capsule is separated from HTV and flies through wide range of flow regime from hypersonic to subsonic speeds. The capsule attitude is controlled by reaction control

Keiichiro FUJIMOTO, Takayuki ITOH, Hideyo NEGISHI, Ryoh NAKAMURA, Yasuhide WATANABE, Kota TANABE

system (RCS) during its lifting descent toward the targeted site and is decelerated to the subsonic speeds. Three thermal protection system (TPS) side shells are separated, and the single ring-sail type main parachute is deployed at the subsonic flow regime, then the capsule will be landed on the Pacific Ocean near Japan and is recovered by ship. As will be described in the following sections in detail, the sample return mission was fully successful in the HTV-7 mission. HSRC has successfully returned from the ISS with the specimens and recovered at the coast of the Ogasawara islands on November 11, 2018 as shown in Figure 1. Comprehensive multi-disciplinary design considerations under the various uncertainties should be carried out to realize reliable Earth-return system. Main challenges of the aerodynamic and aerothermal designs are the thermal protection from the severe aerothermal heating, and the attitude stability control with keeping enough lift-to-drag ratio to keep enough controllability to reach the targeted site precisely. In the current project, the intensive research efforts had been made to investigate the aerodynamic characteristics and the aerothermal heat flux distributions for the wide range of flow conditions. Various computational aerothermodynamic analysis have been carried out in the present study to achieve the aerodynamic stability, the thermal protection from severe aerodynamic heating, the resistance against the aeroacoustics and vibrations, and the reliable parachute deployment.

2. Research Objectives

In this intensive research activity, the aerodynamic and aerothermodynamic design considerations to support the HSRC development have been carried out. Computational fluid dynamics (CFD) analysis have employed for various aerothermodynamics design considerations such as the aerodynamic characteristics and the thermal protection issues. RCS jet interaction with the high temperature main stream and its effect on the aerodynamic characteristics and the local heat-flux increase are investigated. Probabilistic analysis on the trajectory of TPS side shell through unsteady wake behind the capsule is conducted [4]. Aerodynamic stability issues including the side wind criterion for the drop test, and the aero-acoustics characteristics for the unsteady subsonic flows are also investigated [5]. Important findings for the reliability improvement and the related mechanism are comprehensively discussed in detail.

Research objectives in this study are as follows,
- Computational aerothermodynamics design analysis methods and the key findings are overviewed including the results of the previous studies and discussed.
- Post-flight analysis results to validate the models and the assumptions on the design analysis method are presented.
- Key lessons learned, and the further research needs are identified for the future re-entry vehicle missions.

3. HSRC project and HTV-7 mission result

3.1 Overview of the HSRC project and HTV-7 mission result

Objective of the HSRC technology demonstration project is the establishment of the guided lifting re-entry capsule. Current function of the HSRC is to be return-to-Earth capsule to bring the payload such as the specimen from ISS to the Earth. The sample return mission based on HSRC was fully successful in the HTV-7 mission. HSRC has successfully returned from the ISS with the specimens and recovered at the coast of the Ogasawara islands on November 11, 2018 as shown in Figure 1. Demonstrated key technologies are guidance / navigation and control for the lifting re-entry vehicle, Japanese domestic the low weight ablator and the parachute deceleration system. In the HTV-7 mission, the important capabilities of lifting re-entry capsule have been demonstrated [6] as follows,
  1) Precise, pinpoint return-to-Earth capability
     - Down-range errors was 0.51km, and cross-range error was 8.29km as shown in Figure 2.
  2) Reduced aerodynamic acceleration
     - Maximum acceleration level was less than 3.5 G.
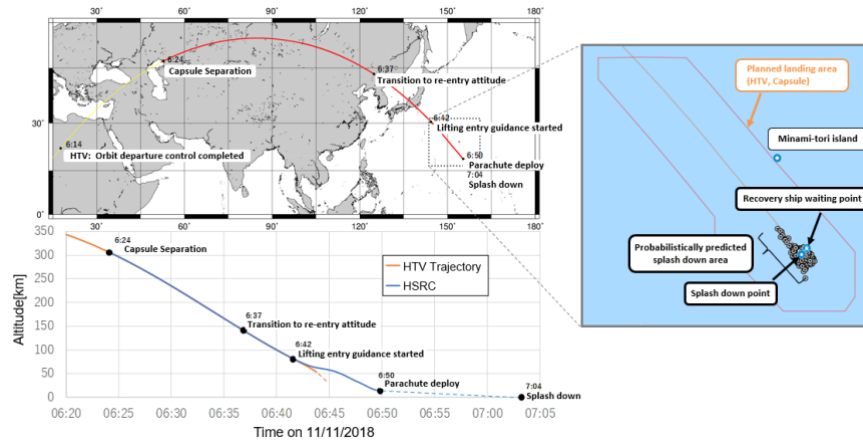
Figure 2: Trajectory, predicted and resulting splash down location for HSRC in HTV-7 mission.

Overview of HSRC sub-systems and the parachute system is shown in Figure 3.
Main features of HSRC are as follows,

a)   Lifting re-entry capsule with single ring-sail type main parachute
b)   Diameter and length are 0.84 and 0.657m, mass is about 200kg including 20kg payloads.
c)   Heat insulated payload container
     (Insulation requirements are 4℃±2℃ and 20℃±2℃ for over 3.5 days)
d)   Ring-sail type main parachute ($D_0 = 7.36$m) designed to be deployed at $11 km$ and $M_\infty = 0.7$.
e)   Eight GN2 thrustors (2.4N vacuum thrust), 4 roll, 2 pitch and 2 yaw thrustors.
f)   Japanese domestic low weight ablator, its density is roughly 0.30 g/cm.
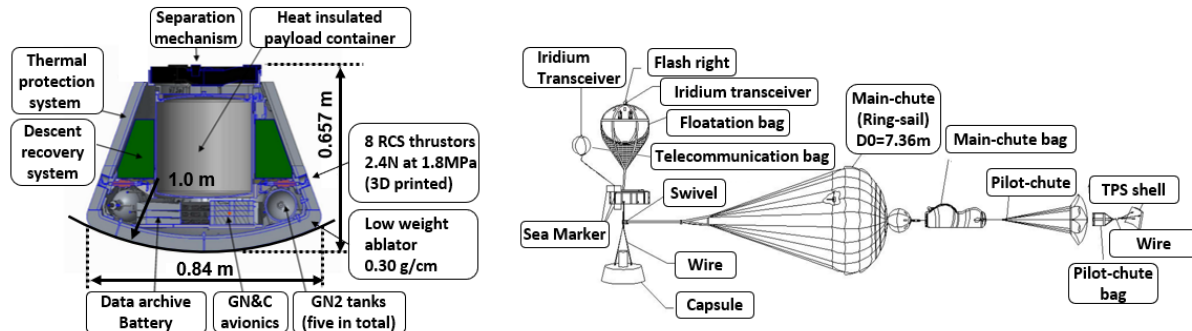
Figure 3: Overview of HSRC sub-systems and the parachute system.

Comparison of the trajectories obtained at the flight measurement and reconstructed in the post-flight analysis is shown in Figure 4. Corresponding stagnation heat flux level evaluated by Detra-Kemp-Riddel equation is also shown for the qualitative understanding on the heat flux level characteristics during the re-entry. In the stagnation heat flux level evaluation, reference length of 1m is used. Re-entry duration time is roughly 7 or 8 minutes, at which the heat flux level is severe. Corresponding free-stream Mach numbers M_∞ are also shown. Maximum free-stream Mach number M_∞ is roughly 27.8.
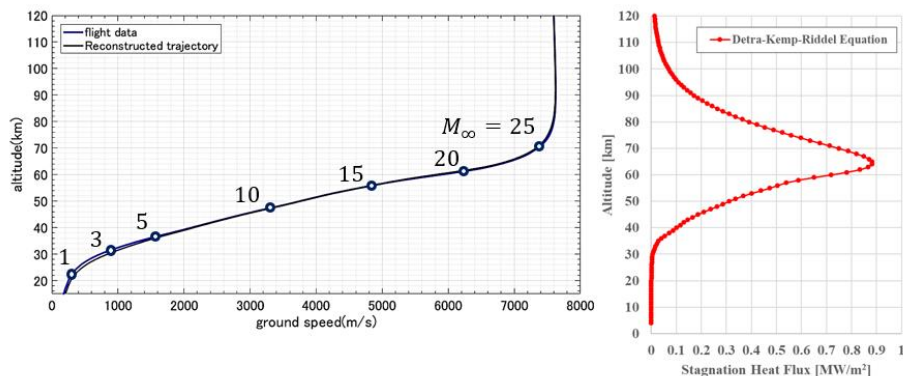
Figure 4: Comparison between the flight and the reconstructed trajectories [6], the stagnation heat flux level.

3

Keiichiro FUJIMOTO, Takayuki ITOH, Hideyo NEGISHI, Ryoh NAKAMURA, Yasuhide WATANABE, Kota TANABE

3.2 Aerothermodynamics design consideration for HSRC development

As shown in the previous section, the re-entry capsule flies under the wide range of flow conditions from the hypersonic, supersonic, transonic, and subsonic regime. Maximum heat flux level at the wind-ward sharp shoulder exceeds above 1.0 MW/m^2. Main challenges of the aerodynamic and aerothermal designs are the thermal protection from the severe aerothermal heating, and the attitude stability control with keeping enough lift-to-drag ratio to realize enough controllability to reach the targeted site precisely.

In summary, major design challenges related to the aerothermodynamics are as follows,
  1) Thermal protection from the severe aerodynamic heating.
  2) Aerodynamic stability with keeping large lift-to-drag ratio.
  3) Precise control for the pin-point landing.
  4) Deceleration by drag during the lifting cruise and the parachute.
  5) Resistance to structure vibration and aero-acoustics wave propagation.
  6) Reliable parachute deployment.

Design consideration and the certification have carried out by the numerical analysis and the experiments in a mutually complementally manner as shown in Table 1. Wind-tunnel facilities of JAXA related to HSRC project [7] are summarised in Figure 5 with the corresponding design consideration items. Various numerical analyses on the aerothermodynamics have been carried out as shown in Figure 6. Various wind-tunnel experiments have been conducted to investigate the flow mechanism and to obtain the aerodynamic and heat flux data. CFD model and its assumptions are validated by the comparison with the wind-tunnel experimental data. Some aspects of the design consideration items have been certified based on the experiments, such as the ablator recession rate and the parachute deployment sequence. For the efficient investigation of the related flow mechanisms and the aerodynamic and heat flux database development, comprehensive design and operation considerations related to the aerothermodynamics are carried out by the CFD [4][5]. Various uncertainties are considered based on the detailed investigation of the flow mechanism and the parametric CFD analysis. Aerodynamic characteristics for the rarefied flow regime is obtained by using direct simulation Monte Carlo (DSMC) analysis is employed. Aerodynamic characteristics in the subsonic through supersonic flow regime are obtained by the wind-tunnel SWT1 and TWT1 experiments and the CFD analysis. For the hypersonic conditions in which the high-enthalpy real gas effect such as the thermal non-equilibrium effect, the high-enthalpy wind-tunnel HWT2 and HIEST experiments are carried out to obtain the aerodynamic characteristics and the heat flux distribution data. In addition, high-enthalpy thermal non-equilibrium CFD analysis by using JONATHAN is also carried out. In order to investigate and quantify the heat flux reduction level and the recession rate for the ablator, 750kW arc-heated wind tunnel (AWT) is used. The dynamic instability problem in the transonic flow regime is an inevitable challenging design problem for the blunt capsule vehicle. Various design considerations such as the parachute deployment timing, capsule's shape, and the control force by the RCS thrusters should be carried out to prevent excessive diverged pitch oscillation due to the dynamic instability. Wind tunnel experiments such as the single degree-of-freedom free-rotation test by transonic wind tunnel TWT1 [8] and the free flight observation by ballistic ranges [9], and numerical analysis [10][11] need to be conducted to establish the dynamic instability design analysis method. Vehicle's lift force is controlled by changing the roll angle based on the RCS thrusters to keep the proper direction of the lift force. Eight RCS thrusters are employed for the HSRC including the wind-ward pitch and roll thrusters. Since the high-enthalpy large dynamic pressure main stream can be interacts with the RCS jet, those can result in the local increasing of the pressure and the heat flux near the around the exit of the RCS nozzle. As will be discussed in the following sections, the hypersonic wind-tunnel HWT2 experiment and the CFD analysis to investigate the RCS interaction mechanism and to obtain the aerodynamic characteristic variation and the increased aerodynamic heating level data. Unsteady pressure sensitive paint (PSP) measurement and the schlieren imaging to obtain the detailed flow variables' distributions are developed and applied to investigate the detailed flow structures. Since there is the little experience on the large size parachute system for the return-to-Earth applications in Japan, fundamental investigations have been carried out to study the mechanism and the behaviour of the parachutes by using the low speed wind tunnel LWT1. Numerical analysis of the flow and structure interaction to investigate the parachute behaviour and the related mechanism has also been carried out [12]. Sequence tests to certify the parachute deployment capability have been conducted by using the LWT1. In addition, since the environmental conditions such as the dynamic pressure level and the direction of the gravity cannot be represented by the wind-tunnel experiment, the high-altitude drop test has carried out for the final certifications.

Table 1: Aerothermodynamics design consideration for HSRC development.

No	Item	Wind tunnel experiment [7] Environmental test	Numerical Analysis	Drop test
1	Heat flux characteristics	● High enthalpy real gas effect (HWT2 and HIEST)	● CFD	
2	Ablator certification	● Ablator recession rate AWT		
3	Aerodynamic characteristics (*1)	● Subsonic to supersonic (SWT1 and TWT1) ● High enthalpy real gas effect (HWT2 and HIEST)	● CFD, DSMC Modified Newtonian	
4	Dynamic stability	● TWT1[8], Ballistic range [9]	● CFD [10][11]	
5	RCS thrustor interaction	● HWT2	● CFD	
6	Venting characteristics		● CFD Venting Model	
7	TPS shell separation	● Sequence test (LWT1)	● CFD [4]	●
8	Parachute deployment	● Sequence test (LWT1)	● FSI [12]	●
9	Aeroacoustics	● Acoustics vibration test	● CFD [5]	

*1: Aerodynamic characteristics database was developed including the shape change effect due to the ablation loss, the measurement uncertainty and the aerodynamic derivatives.

750 kW arc-heated wind tunnel (AWT)

1m×1m Supersonic Wind Tunnel (SWT1)
2m×2m Transonic Wind Tunnel (TWT1)

High enthalpy shock tunnel (HIEST) **Transonic ballistic range** **6.5m×5.5m Low-Speed Wind Tunnel (LWT1)**
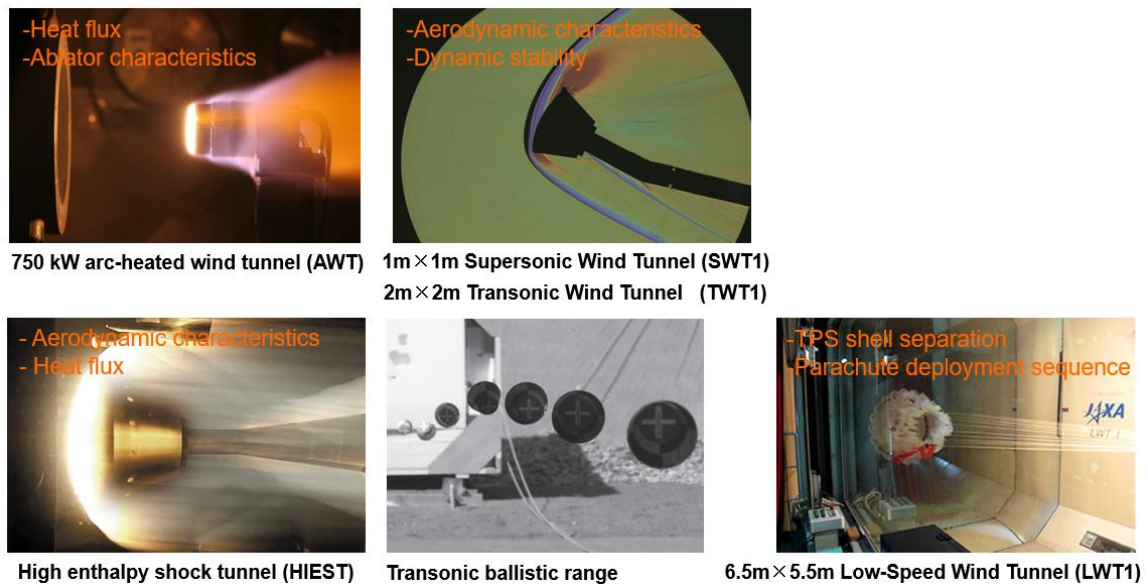
Figure 5: Wind-tunnel experiments for HSRC development [7][8][9].
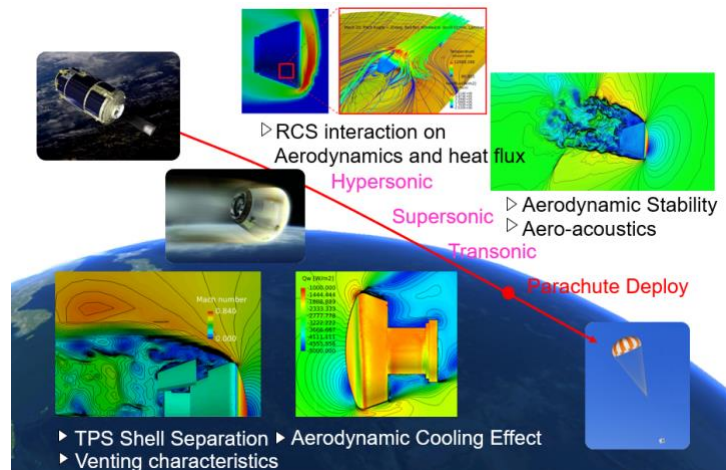
Figure 6: Numerical analysis on the aerothermodynamics for HSRC development.

Keiichiro FUJIMOTO, Takayuki ITOH, Hideyo NEGISHI, Ryoh NAKAMURA, Yasuhide WATANABE, Kota TANABE

3.3 CFD code of JAXA

As discussed in the previous sections, the numerical analysis such as the CFD is essential to investigate the flow structures and to obtain the aerodynamic characteristics and the heat flux distributions. Since wide range of flow conditions should be considered, the large number of the parametric study is essential to consider the various uncertainties. In this research activity by the present authors, two CFD codes LS-FLOW and JONATHAN are applied. LS-FLOW is mainly applied to the subsonic through supersonic flow regime, and JONATHAN is applied to the hypersonic flow regime to consider the high-enthalpy real gas effect.

Numerical schemes employed in the LS-FLOW [4][5] are summarized in Table. LS-FLOW is the compressible Navier-Stokes solver for the unstructured arbitrary polyhedral meshes, and Favre averaged Navier-Stokes equations for compressible flow are solved by the finite volume method. LS-FLOW is one of the main CFD code of JAXA, which is initially developed by present author [13] and has been improved, various numerical schemes have been implemented [14]. LS-FLOW has been applied to various problems including aerodynamic analysis [14], high temperature reactive flows for rocket engine chambers, and the cryogenic flows. In order to expand the applicable fluid dynamics fields, the comprehensive research effort has been made to develop the state-of-the-art accurate physical models, and then those models are quickly implemented into this code for the timely contribution to JAXA's projects. Validation study has also been conducted for the projectiles such as rockets and the blunt bodies such as spheres [15] and Apollo command module [14]. Most of the computational grids used in this research activity are body-fitted Cartesian grid generated by the LS-GRID [16]. In this approach, Cartesian grid is used to fill the volume over the body and the body fitted layer grid is used to resolve the high-Reynolds number boundary layers. Since the aerodynamic characteristics and the heat flux distributions in the wide range of flow regime should be considered, the detached shock wave and the unsteady wake flow behind the capsule should be resolved accurately. Since Cartesian grid cell can be divided into smaller cells with keeping mesh quality, this adaptiveness depending on the flow structures' scale would be the strong advantage to realize an efficient parametric CFD analysis. As will be discussed in the following sections, the spatial accuracy to resolve the unsteady wake flow is essential to realise quantitative evaluation of the aerodynamic characteristics especially for the subsonic and transonic flow regimes.

Numerical schemes employed in the JONATHAN are summarized in Table 3. JONATHAN is the thermal non-equilibrium flow solver for the multi-block structured meshes [17]. It has been developed for the multi-component high-temperature reacting flows for the use in aerospace applications. JONATHAN is designed to be applied to the assessment of the planetary entry environment with ablation of the thermal protection system and radiative heat transfers. Currently, 32 gas species and corresponding chemical reactions, the multi-temperature thermodynamics, and the accurate heat and mass transport models can be considered. It has been widely applied to the planetary entry analysis such as the Mars entry vehicle including RCS jet interaction [17].

Table 2: Numerical schemes implemented for LS-FLOW [4][5].

Governing equations	3D compressible Navier–Stokes equations (Cell-centered FVM)
Grid	- Arbitrary polyhedral meshes, Overset, 6DoF - Immersed Boundary method - Adaptive mesh Refinement (AMR)
Chemical reaction	Models for LOX/LH2, N2H4/NO2, and so on.
Equation of state	Ideal, SRK-based (Sub/Super critical)
Spatial reconstruction	- Green-Gauss, WLSQ, LSQ with various limiter functions - High order reconstruction for unstructured meshes
Inviscid term	- Roe, AUSM-type, SHUS, SLAU - Preconditioned schemes
Viscous term	Shima's and Wang's Method
Turbulence	Baldwin-Lomax, SA, SST, DES/DDES, LES
Time integration	- 2nd order LU-SGS, Block LU-SGS, preconditioned - ERENA for Reactive flows

Table 3: Numerical schemes implemented for JONATHAN [17].

Governing equations	3D compressible Navier–Stokes equations
Grid	- Multi-zonal Structured Grid
Thermochemical model	- Park's two temperature model - 6 Reaction model, 6 Species (N2,O2,NO,N,O,Ar) - Landau-Teller type Vibrational Relaxation model - Preferential Dissociation model (Averaged energy dissociation and recombination molecular is assumed to be 30% of dissociation energy)
Transport coefficients	Viscosity: Blottner Heat transfer: Eucken eq. Diffusion: Sc=0.5
Spatial reconstruction	MUSCL 2nd order accuracy
Inviscid term	AUSM-DV, AUSM^{+}-up, SLAU, SLAU2
Turbulence	LES RANS: Baldwin-Lomax, Spalart-Allmaras, SST model
Time integration	- 1st order Explicit Euler method + Diagonal point implicit method - Runge-Kutta explicit, LU-SGS implicit

4. Analysis conditions

Geometric parameter values considered in this analysis are shown in Figure 7. Geometry considered in the RCS interaction analysis and the aeroacoustics analysis is on the left, and the geometry considered in the TPS shell separation analysis in on the right. Some of the parameter difference of the leeward cylindrical part is due to the design update depending on the development phase. Flow conditions considered in the design analysis are compared with the reconstructed trajectory data based on the post-flight analysis of HTV-7 mission as shown in Figure 8 and Figure 9. Two different trajectories are considered in the RCS interaction analysis, the one is lower lift-to-drag ratio (L/D) case and the other is higher L/D case. Dynamic pressure magnitude for the lower L/D becomes larger as comparing with the higher L/D case. As it is well known that the dynamic pressure, the mass flow rate and momentum of the free-stream have strong influence on the local pressure and heat flux increase induced by the RCS-jet interactions. The corresponding stagnation heat flux level evaluated by the Detra-Kemp-Riddel equation is also shown in Figure 8. It is found that the flight trajectory of HTV-7 is just between the lower L/D trajectory and the higher L/D trajectory. Thus, the corresponding stagnation heat flux level is also within the rage between the lower L/D case and higher L/D case. Flow conditions considered in the aeroacoustics analysis and the TPS shell separation analysis are also shown in Figure 9 including the comparison with the HTV-7 flight data. Averaged dynamic pressure level considered in the design analysis is higher than that of flight data. Since the aeroacoustics level is proportional to the dynamic pressure, thus the design analysis assumption would be the worst-case assumption. In addition to this margin, input sound pressure level (SPL) for the acoustics vibration test is selected with additional margin on the SPL magnitude. In general, it is found that the considered flow conditions are worst-case assumption as comparing with flight conditions.

Keiichiro FUJIMOTO, Takayuki ITOH, Hideyo NEGISHI, Ryoh NAKAMURA, Yasuhide WATANABE, Kota TANABE
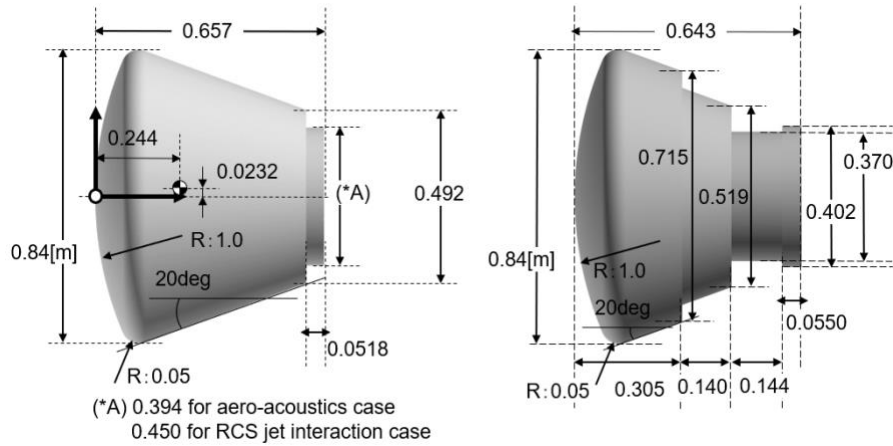
Figure 7: HSRC configurations considered in CFD.
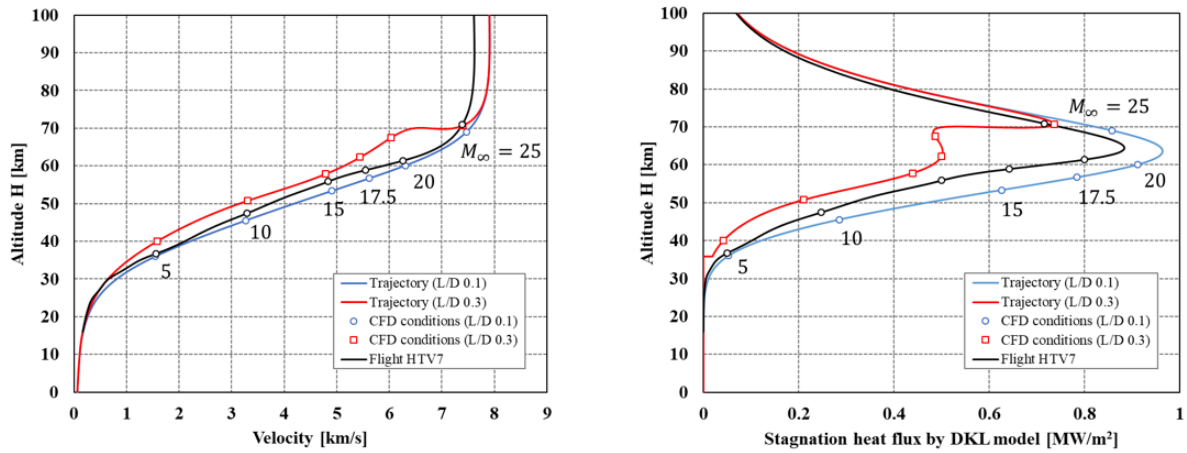
Figure 8: Trajectory conditions for RCS-jet interaction analysis.
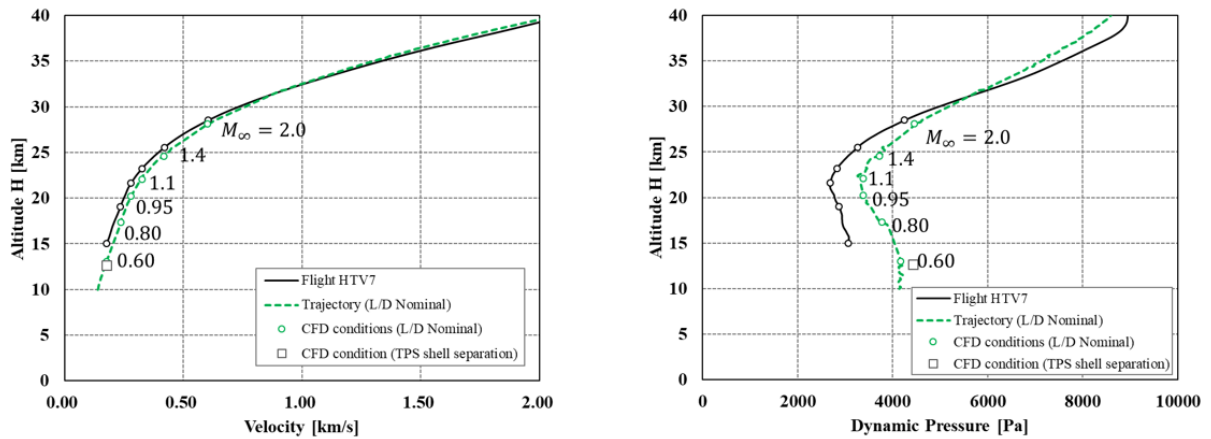
Figure 9: Trajectory conditions for aeroacoustics and TPS shell separation analyses.

5. Result and discussions

Computational aerothermodynamic design analysis methods and the key findings are discussed. Contributions of this research activity to the success of the HTV-7 mission are summarized based on the post-flight analysis results.

5.1 RCS Jet Interaction on Aerodynamics and Heat flux

HSRC is equipped with the 8 RCS thrusters, 2 pitch thrusters, 2 yaw thrusters and 4 roll thrusters respectively. One of the pitch thrusters and the two of the roll thrusters are located on the wind-ward side, and the flow separation is not occurred at the wind-ward capsule's shoulder. Therefore, the large dynamic pressure and high temperature main-stream collides with the RCS jet coming from the nozzle exit. It is resulting in the local heat flux and the pressure increase around the RCS nozzle exit. The local heat peaks and the pressure increase are resulting in the non-linear variation of the aerodynamic characteristics and the heat flux distributions. Since the pressure and the heat flux increase levels are highly depending on the flow conditions, such characteristics should be analysed for each possible trajectory conditions. Windward pitch and roll RCSs are considered in the design analysis, results for the pitch RCS are discussed. Considering the high-enthalpy real gas effect is essential to predict the aerodynamic characteristics and the heat flux change. Therefore, JONATHAN is applied to this analysis, and the employed schemes are summarized in Table 4. Multi-block structured computational grid is shown in Figure 10. Total cell number is roughly 1.6 million, the minimum grid spacing size is set as the cell Reynolds number to be less than 1.0. As already described in the section above, two different trajectories are considered. One is the larger dynamic pressure cases as shown in Table 5, and the other is the smaller dynamic pressure cases as shown in Table 6.

Table 4: Numerical schemes of JONATHAN employed for RCS jet interaction analysis.

Governing equations	Compressible 3D Navier-Stokes equations
Chemical species	6 Species model (N2, O2, NO, N, O, Ar) by ASRC36-07-AB03, KeqCNO-05b Source term for dissociation/recombination (preferential dissociation α=0.3) Two temperature model (Ttrn-rot, Tvib-exc-etr) [18] Landau-Teller vibrational energy relaxation (without park's modification) [19]
Transport properties	Viscosity: Blottner [20], Conductivity: Eucken [21], Diffusion: Sc=0.5
Turbulence model	Laminar
Euler flux	AUSM-DV [22]
Reconstruction	2nd order MUSCL [23]
Time integration	1st order explicit Euler time integration + diagonal point implicit method [24]

Total : 1.6 million cells for half body
$(10 \times 10 \times 100) \times 160\ Block$
Minimum grid size: $1.0 \times 10^{-6}[m]$
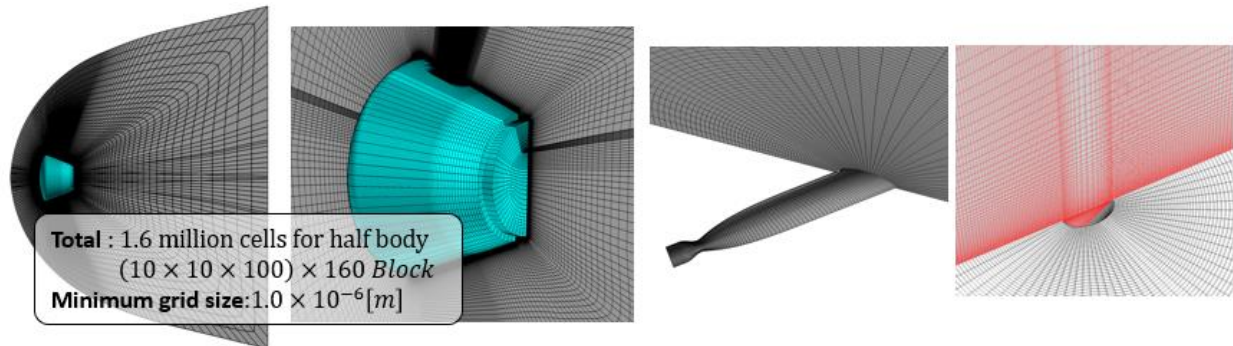
Figure 10 Multi-block structured grid generated for RCS interaction analysis.

Table 5: Larger dynamic pressure trajectory conditions for RCS interaction analysis.

Mach number M_∞	5.0	10.0	15.0	17.5	20.0	25.0
Reynolds number Re_∞*1	6.093×10^5	3.044×10^5	1.603×10^5	1.365×10^5	9.519×10^4	3.723×10^4
Altitude $[km]$	36.009	45.546	53.347	56.692	60.090	70.670
Velocity $U_\infty\ [m/s]$	1550.6	3270.3	4900.5	5615.8	6300.4	7392.1
Pitch angle $[deg]$	20					

*1 Reference length of the Reynolds number is maximum diameter of the capsule 0.84m.

Table 6: Smaller dynamic pressure trajectory conditions for RCS interaction analysis.

Mach number M_∞	5.0	10.0	15.0	17.5	20.0	25.0
Reynolds number Re_∞	4.483×10^5	1.748×10^4	9.427×10^4	7.323×10^4	6.075×10^4	2.165×10^4
Altitude $[km]$	38.075	49.689	58.334	61.746	63.996	72.106
Velocity $U_\infty\ [m/s]$	1568.1	3297.9	4769.7	5461.5	6160.8	7337.2
Pitch angle $[deg]$	20					

Keiichiro FUJIMOTO, Takayuki ITOH, Hideyo NEGISHI, Ryoh NAKAMURA, Yasuhide WATANABE, Kota TANABE

Predicted Mach number distributions in the symmetry plane and the surface pressure distributions for smaller dynamic pressure case (L/D 0.3) are shown in Figure 11. Closeup views of the surface pressure and the heat flux distributions near RCS nozzle exit are also shown in the bottom figures. It is not shown as the figure due to the space limitation, however the observed flow structure is typical jet-in-cross flow structure in which the detached shock wave is generated aft of the jet and the hose-shoe type vortex is also generate around the jet. As a result, the local pressure and the heat flux increase is observed, and those influenced area are much larger than the RCS nozzle exit area. For the investigation of its significance, the variations of the aerodynamic axial and normal force and the pitching moments for each flow conditions are shown in Figure 12. Variations of the axial force, the normal force and the pitching moment are ΔF_x, ΔF_z, and ΔM_p respectively. Its coordinate definition is also shown in Figure 11. Magnitude of the ΔF_x is more than 6 N, and the magnitude of the ΔF_z is more than 10 N. Magnitude of the ΔM_p is roughly 2 Nm. Since the vacuum RCS thrust is about 2.4 N, and thus the RCS jet interaction effect is significant. Although the vehicle velocity is decelerated at the lower altitude, the mass flow rate is getting larger at the lower altitude due to the increase in the atmospheric density. In the larger mass flow rate case, the area of the local pressure increase becomes larger as shown in Figure 11 $M_\infty = 5.0$ case. Therefore, all magnitudes of variations on the aerodynamic force and moments becomes larger with the mass flow rate decrease. Mass flow rate is defined as the RCS jet mass flow divided by the incoming free-stream's mass flow rate evaluated by using capsule's projection area. Maximum heat flux at the wind-ward shoulder and the local heat peak by the RCS jet interaction for smaller dynamic pressure trajectory case are shown in Figure 13. Wind-ward pitch RCS thruster is considered. Augmentation factor [32] (AF) is also shown in the same figure. AF is defined as the local heat peak value divided by the heat flux level without the RCS jet interactions. Since the stagnation enthalpy is much larger for the large Mach number cases such as $M_\infty = 20$ and 25, the maximum heat flux is larger at those conditions. However, the local heat peak by RCS jet interaction does not increase with the free-stream enthalpy. Its upper bound is roughly 0.25 MW/m^2 observed at $M_\infty = 15, 17.5$ and 20. Values of AF are roughly 8 at $M_\infty = 5$ and 2 at $M_\infty = 25$, and it gradually increases with Mach number decrease. It is mainly due to the free-stream mass flow rate increase.
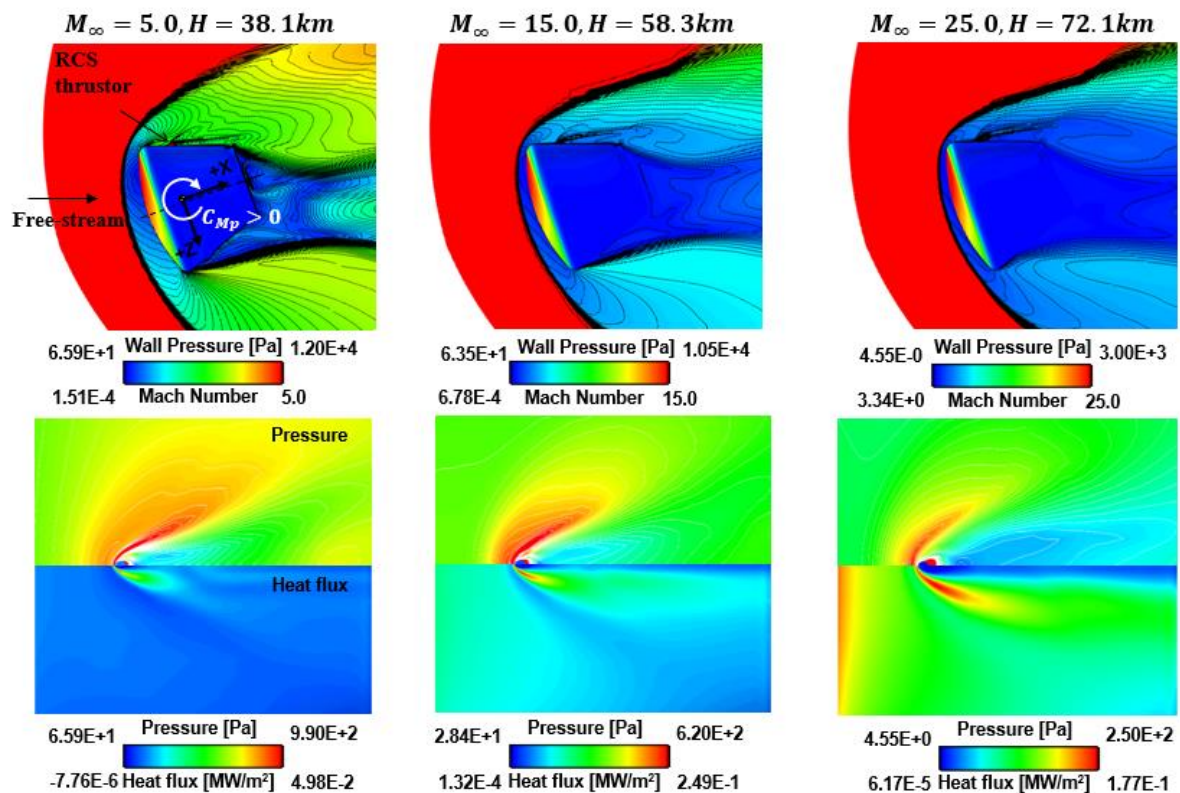
Figure 11: Windward pitch RCS jet and free stream interaction on the aerodynamic characteristics and the heat flux.
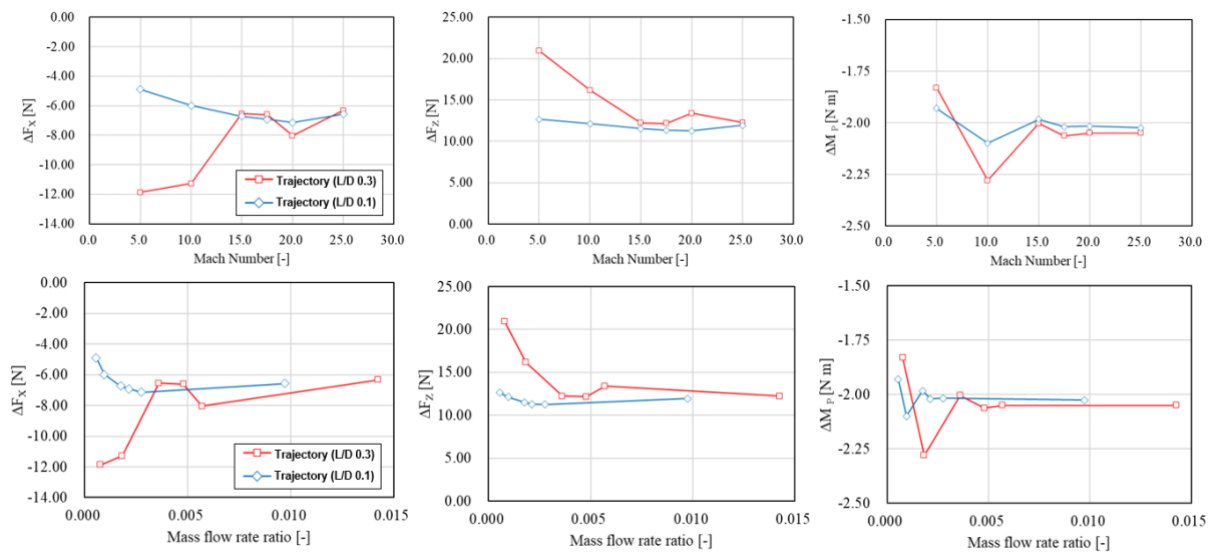
Figure 12: Windward pitch RCS jet interaction effects on the aerodynamic force and moments.

It was found that the RCS jet interaction effect on the aerodynamic characteristics and the local heat flux increase is significant. Thus, the regression models to describe the variations in the aerodynamic coefficients are constructed based on M_∞ and the mass flow rate. Those variation in the aerodynamic coefficients are considered by using those regression models in the probabilistic GNC trajectory analysis. Local heat flux peak generated by the RCS jet interaction is also significant, and thus the additional ablator disk is re-designed to be located to protect the top face of the 3D printed RCS thruster module as shown in Figure 14. From the detailed analysis on the recovered flight hardware, severe thermo-mechanical erosion of the ablator was not found. Furthermore, although it is indirect evidence, however, unexpected vehicles' acceleration was not found from the flight measurement data. Aerodynamic disturbances due to the RCS jet interaction are considered to be within the expectation as much as investigated in the post-flight analysis.
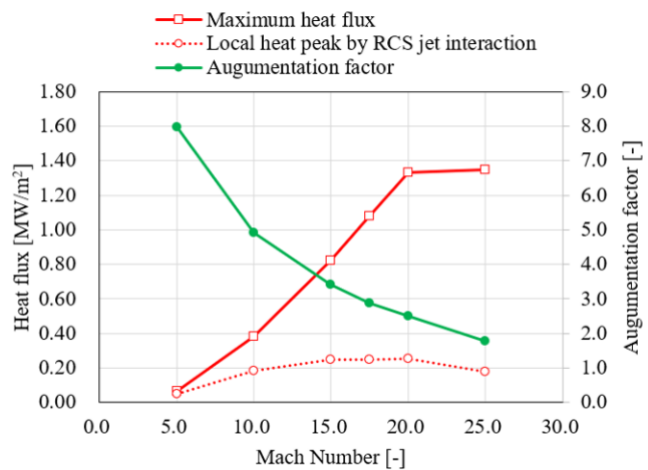
Figure 13: Windward pitch RCS jet interaction effect on the heat flux for smaller dynamic pressure trajectory.

Figure 14: Windward ablator of the recovered HSRC.

Keiichiro FUJIMOTO, Takayuki ITOH, Hideyo NEGISHI, Ryoh NAKAMURA, Yasuhide WATANABE, Kota TANABE

5.2 Venting air characteristic analysis

Venting the air to balance the pressure difference between the internal and atmospheric pressure is essential to prevent the structural and the TPS shell separation failures. Since the temperature over the capsule becomes significantly larger during the hypersonic flow regime, incoming heating by the hot gas injection should be considered to prevent the thermal damage on the avionics and the parachute thin materials. In order to achieve the balance between the pressure difference and the incoming heating, the venting air characteristics analysis is carried out. Venting hole is designed to be located on the lee-ward cylindrical end-face to prevent direct injection of the hot gas with the large dynamic pressure. For the damping of the pressure fluctuation and to temperature reduction of the hot gas, the fibrous insulation and the multiple orifice plate are employed for HSRC as shown in Figure 16. Venting characteristics analysis method is developed in which coupling analysis is performed based on the time-history data of the pressure and the temperature at the vent hole obtained by CFD and the 1D Euler flow analysis model to evaluate the internal pressure characteristics and the incoming heat as shown in Figure 15. Effects of the venting hole area and the contraction coefficient on the internal pressure change and the incoming heat due to the hot gas injection were analysed and those design values were decided based on the analysis results to prevent the damage of the avionics and the parachutes.
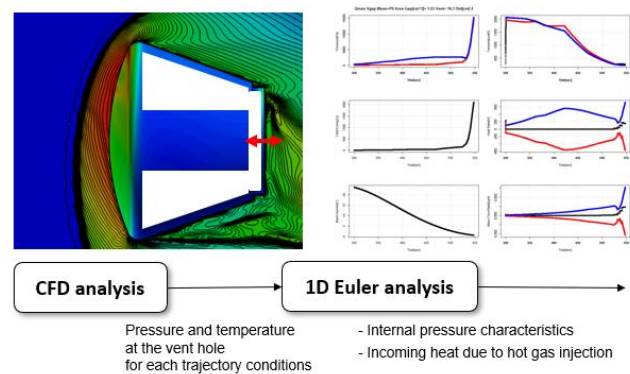
Figure 15: Venting air characteristics analysis model.

Figure 16: Hatch attachment side view of recovered HSRC.

Return-to-Earth mission of HSRC on HTV-7 was successful without any failure related to the venting air issues. Major findings from the from the detailed analysis of the flown hardware are shown bellows.

1) Internal structure melting is not observed.
2) Unexpected temperature increase due to the incoming hot gas was not observed.
3) Predicted maximum heat flux level for the windward shoulder
   is in quantitatively good agreement with the re-entry flight data.

5.3 Aeroacoustics induced by unsteady wake [5]

During the supersonic through subsonic flow regime, the dynamic pressure level of the leeward of the capsule becomes larger. Unsteadiness of the shear layer separated from the shoulder becomes stronger due to the local shock wave interaction over the shear layer. Since there are little previous investigations and the little experience to certify the resistance to the acoustic vibrations, the unsteady CFD analysis is carried out in the present authors' previous studies. One of the objectives of this report lies in the overviewing all computational aerothermodynamics design analysis to support the HSRC development. Research result of the previous study [5] is briefly described. LS-FLOW was employed in this study, and selected numerical schemes are shown in Table 7. Since it has the advantages to resolve the small-scale vortices in the unsteady wake by using the adaptively refined Cartesian grid, the body-fitted Cartesian grid generated by LS-GRID was used as shown in Figure 17. Total number of cells is roughly 9.3 million. Flow conditions used in this analysis are summarized in Table 8. MILES-type analysis based on the conventional turbulence model was used. Predicted pressure fluctuation characteristics is in good agreement with the wind-tunnel experiment including both the location and the Mach number dependencies [5]. Predicted instantaneous the Mach number distributions in the symmetry plane and the surface pressure distributions are shown in Figure 18. Time-averaged Mach number distributions in the symmetry plane and the stream lines on the surface and in the symmetry

plane are also shown in the middle column in Figure 18. During the transonic flow regime, the local shock wave is generated over the shear layer which is resulting in the large surface pressure fluctuation induced by the unsteady shear layer. It can be also found from the stream lines in the symmetry plane that the velocity magnitude of the adverse flow has significant dependency on the location and the flow conditions. Corresponding SPL distributions over the leeward surface are also shown in Figure 18. Predicted root mean square (RMS) of the surface pressure fluctuations p_{RMS} is shown in right side of Figure 19. p_{RMS} is normalized by free-stream dynamic pressure q_∞. Maximum, mean and minimum among the selected locations defined in right figure of Figure 19, and the global mean of leeward surface are compared. Computed results for flat-faced base flow obtained by Kawai et al [33] are also shown in same figure. Normalized RMS becomes significantly large for the transonic and subsonic cases as comparing with the supersonic case. Normalized RMS of the surface pressure fluctuation generally decreases with the Mach number increases, local peak is observed for $M_\infty = 0.95$. In addition, there are large difference between the results for the capsule and the cylinder base flow especially at subsonic conditions. The normalized RMS for capsule is roughly twice as comparing with that for the base flows. After the validation of the CFD analysis of the pressure fluctuations by the comparison with the wind-tunnel experiment data, the time-history data of the surface pressure fluctuation was obtained. Then, the frequency spectrum of sound pressure level is obtained for each position over the surface. Finally, SPL level for the acoustics vibration test was decided including the additional margins. Configurations for the acoustics vibration test for the flight model is shown in Figure 20.

Risk of the structure and the avionics damage due to the acoustics vibration has investigated to be small based on the acoustics vibration test. This is mainly due that most of the induced vibration energies are damped through the thick and heavy structure. Damage related to the acoustics vibration is not found from the recovered HSRC hardware, as well.

Table 7: Numerical schemes of LS-FLOW employed for the aeroacoustics and the drop test trajectory analyses.

Governing equations	Favre-averaged compressible 3D Navier-Stokes equations
Turbulence model	Baldwin-Lomax model [25]
Reconstruction	Green-gauss, 2nd order [26][27] Venkatakrishnan limiting function [28]
Euler flux	SLAU [29]
Viscous flux	Shima's method
Time integration	LS-SGS implicit scheme [30] 2nd order with inner iteration with 4 Inner iterations
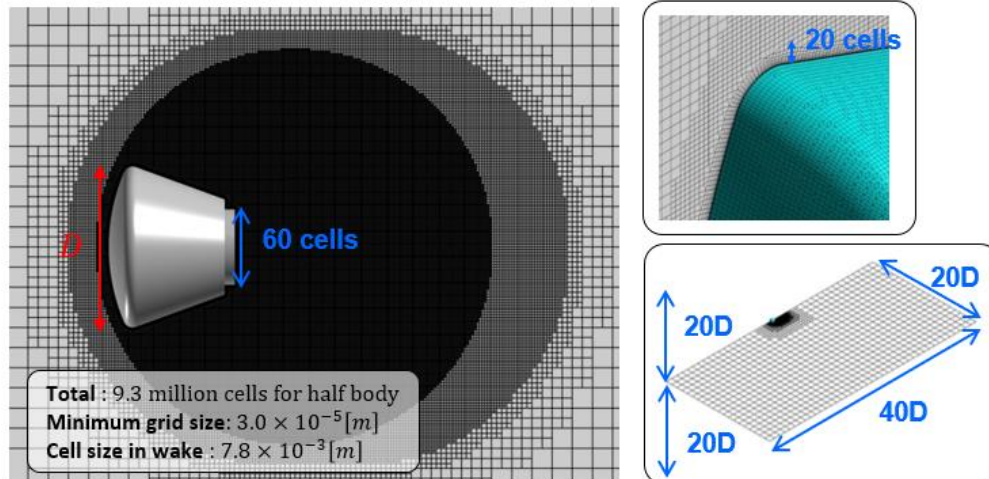
Figure 17: Body-fitted Cartesian grid for the aeroacoustics and the drop test trajectory analysis.

Table 8: Flow conditions for aeroacoustics analysis.

Mach number M_∞	0.60	0.80	0.95	1.1	1.4	2.0
Reynolds number Re_∞	2.76×10^6	1.87×10^6	1.41×10^6	1.21×10^6	1.03×10^6	8.45×10^5
Altitude $[km]$	13.03	17.32	20.22	22.09	24.59	28.12
Velocity U_∞ $[m/s]$	177.04	236.06	280.42	326.08	417.36	600.93
Pitch angle $[deg]$	20					

Keiichiro FUJIMOTO, Takayuki ITOH, Hideyo NEGISHI, Ryoh NAKAMURA, Yasuhide WATANABE, Kota TANABE
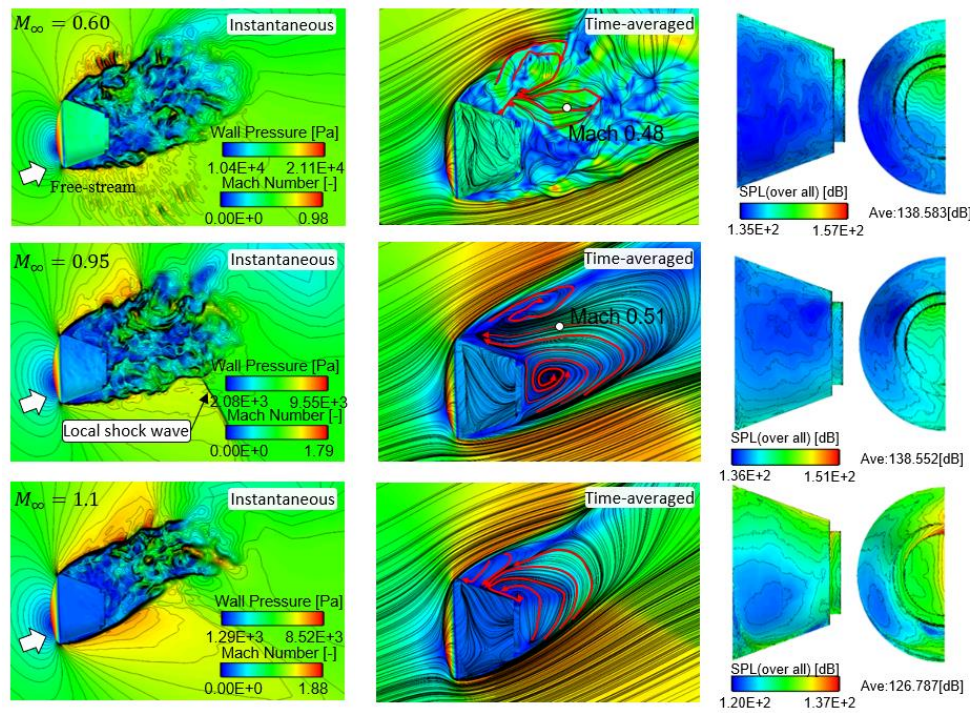
Figure 18: Instantaneous and time-averaged flow structures and sound pressure level over the surface [4].
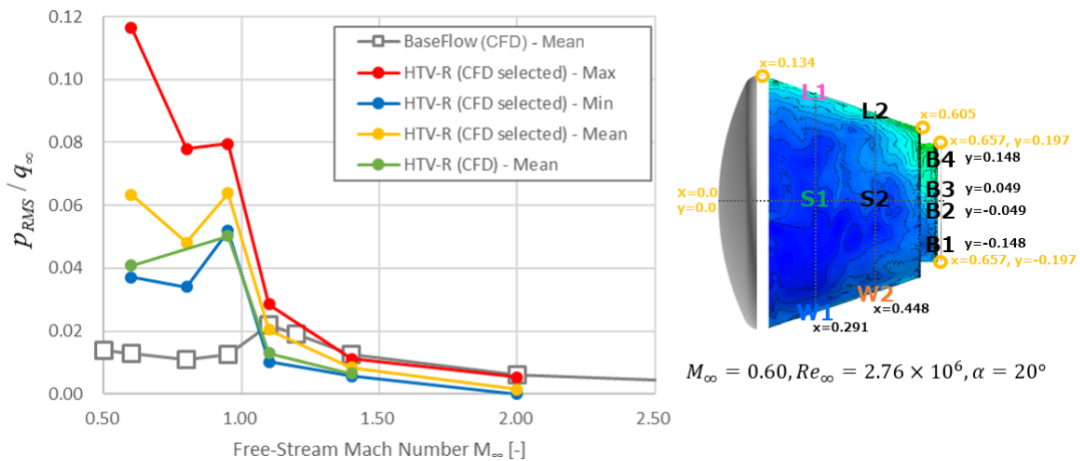
Figure 19: Computed root mean square of surface pressure fluctuations [4].

Figure 20: Acoustics vibration environmental test for the HSRC flight model.

5.4 Probabilistic TPS shell separation behaviour in unsteady wake [4]

Configuration of the parachute system is shown in Figure 3. Parachute deployment timing is designed to be subsonic flow condition ranging from $M_\infty = 0.6$ to 0.7. TPS shells are initially separated from the capsule, the pilot-chute bag is connected to one of the TPS shells by the wire. Pilot-chute bag is dragged by the aerodynamic force of the connected TPS shell. Therefore, the reliable TPS shell separation is essential for the parachute deployment success. As already discussed in the previous section, the unsteadiness of the wake flow behind the capsule becomes larger in the transonic and subsonic flow regime. In addition, adverse recirculating flow can cause the TPS shell's separation failure. In addition, the active devices to generate the large separation force such as the pyrotechnics and the spring cannot be employed due to the difficulty to achieve the redundant fail-safe capability to prevent crew injury during the payload operation inside the ISS. Furthermore, since the TPS shell is initially located in the unsteady wake flow and its attitudes are also uncertainty factor. Therefore, the probabilistic TPS shell's trajectory analysis method with considering the various uncertainty factors has been developed in the present author's previous study [4]. Aerodynamic coefficients of the TPS shell for each location with respect to the capsule and its attitude are obtained by the CFD. Conventional MILES-type analysis by LS-FLOW is employed for this analysis. Selected numerical schemes for this study are summarized in Table 9. Flow conditions considered in this study is summarised in Table 10. Including the TPS shell location in the axial and radial directions, roughly more than 80 CFD analysis have been conducted. Based on the aerodynamic characteristics obtained by CFD, the regression models to approximate the location and the pitch angle dependency are constructed based on the Kriging regression as shown in Figure 22. Then, 3DoF TPS motion of equations are solved by using the location and pitch angle dependent aerodynamic characteristics. Requirement for the separation conditions such as the initial velocity and the pitch angle can be evaluated for the success of the separation against the adverse recirculating flow. Predicted aerodynamic characteristics depending on the TPS shell location for the pitch angle 0 are shown in Figure 22. Initial position of the TPS shell's center-of-gravity before the separation is also shown as red-circle in the same figure. Lift, drag and pitch moment are all negative just after the separation due to the adverse recirculating flow. Even after the TPS shell reaches shear layer location, it was found that the direction of the aerodynamic force can be the adverse toward the capsule [4]. It has been shown that the TPS shell's collision and the separation failure risks are significant by the probabilistic design analysis. For those risk mitigations, TPS shell release air-bag has been adopted to enforce the TPS shell to be separated by the inflated air bag as shown in Figure 23.

It has been shown from the detailed analysis of the flight data and the recovered hardware that,
1) TPS shells are separated by the inflated release bag.
2) Severe collision of the TPS shell with the capsule was not observed.
3) Since the parachute deployment failure can be directly result in the capsule recovery failure, the significant importance of the release bag is confirmed by the post-flight analysis.

Table 9: Numerical schemes of LS-FLOW employed for the TPS shell separation analysis [4].

Governing equations	Favre-averaged compressible 3D Navier-Stokes equations
Turbulence model	Baldwin-Lomax model [25]
Reconstruction	Green-gauss, 2nd order l [26][27] Venkatakrishnan limiting function [28]
Euler flux	SLAU [29]
Viscous flux	Shima's method
Time integration	LS-SGS implicit scheme [30] 2nd order with inner iteration with 8 Inner iterations
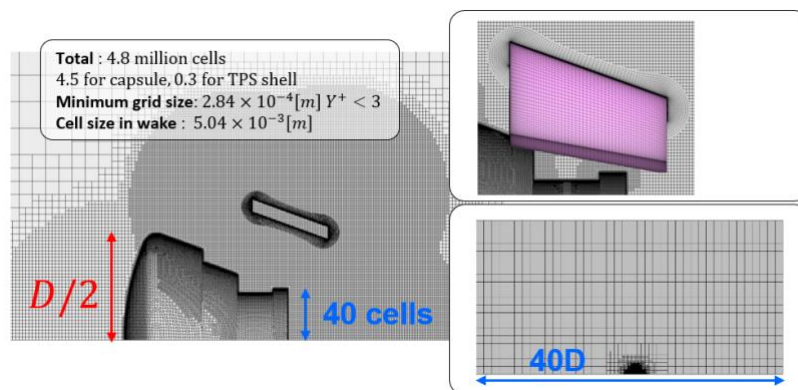
Figure 21: Body-fitted Cartesian grid for the capsule and the over-set hexahedral mesh for TPS shell [4].

Keiichiro FUJIMOTO, Takayuki ITOH, Hideyo NEGISHI, Ryoh NAKAMURA, Yasuhide WATANABE, Kota TANABE
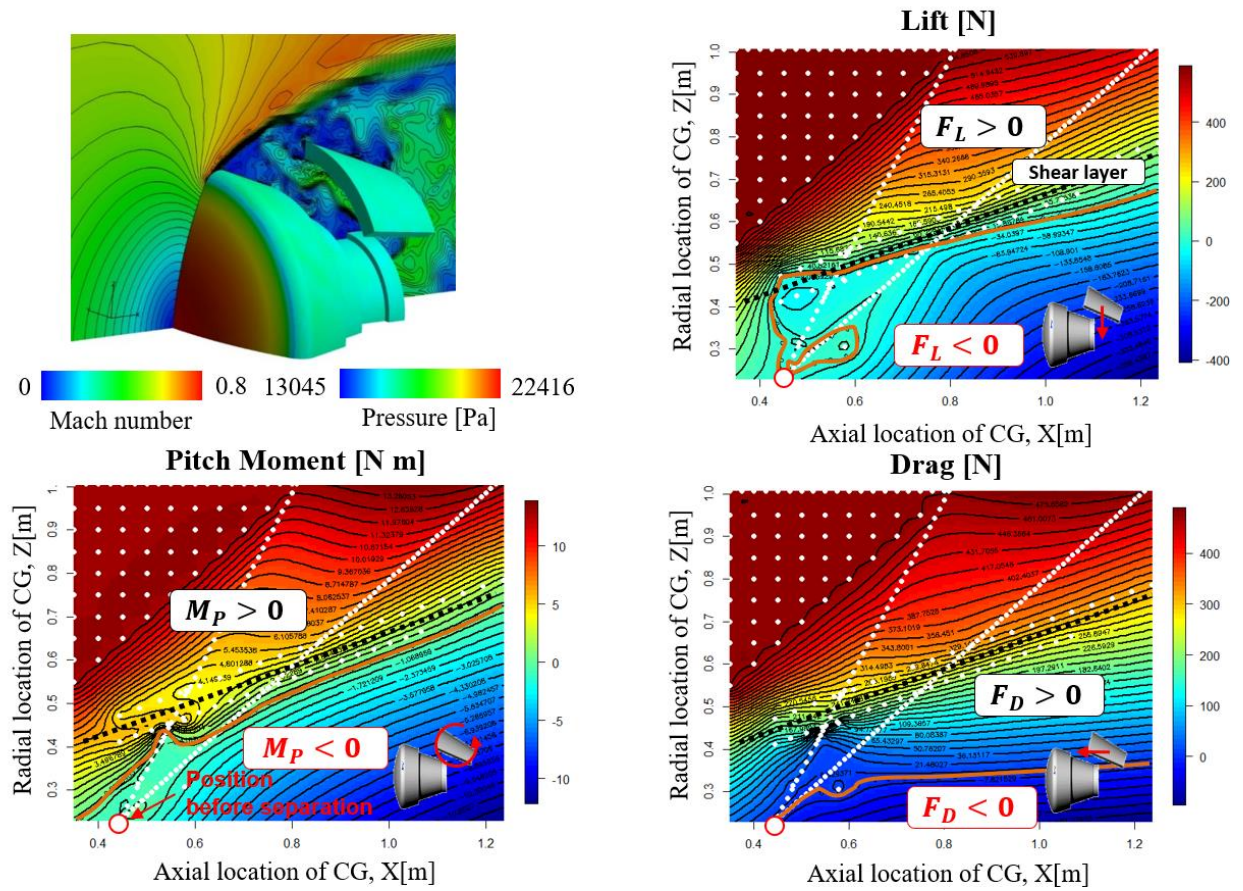
Figure 22: Location dependencies on the aerodynamic force and pitch moment for TPS shell at pitch angle 0 [4].

Table 10: Flow conditions for TPS shell separation analysis [4].

Mach number M_∞	0.60
Reynolds number Re_∞	2.95×10^6
Altitude [km]	12.632
Velocity U_∞ [m/s]	177.02
Pitch angle [deg]	$-70\ to\ 30$
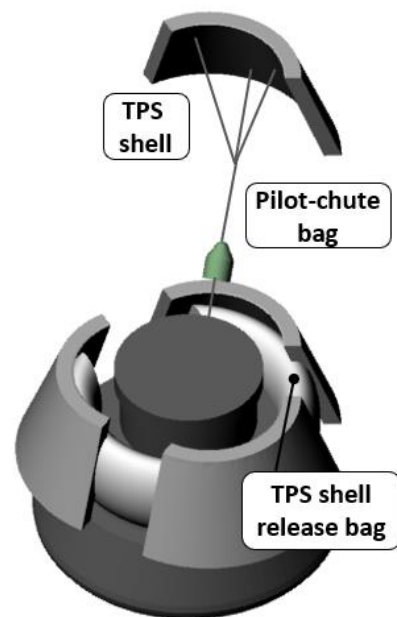
Figure 23: TPS shell release bag for the reliable separation.

16

5.5 6DoF probabilistic trajectory analysis for the drop test

Multiple high-altitude drop tests have been conducted for the system certifications throughout the entire sequence such as the parachute system deployment, the decent and the recovered by the collecting ship. In the initial phase just after the capsule separation from the helicopter, the pitching turn-over rotation has been observed in the drop test at earlier development phase. Probabilistic 6DoF trajectory analysis is carried out to clarify its root cause. By using the LS-FLOW with the selected numerical schemes as shown in Table 7, the aerodynamic characteristics is obtained for the flow conditions as shown in Table 11. Mach number dependency on the aerodynamic characteristics assumed to be negligible, and thus only the $M_\infty = 0.15$ case is considered. Aerodynamic coefficients for $M_\infty = 0.15$ are used for all free-stream Mach numbers. Body-fitted Cartesian grid as shown in Figure 17 is used in this study. Based on the aerodynamic coefficient database predicted by CFD, the 6DoF equation of motions are solved with including the side wind effect. Pitching moment induced by the small parachute attached on the edge of sling is modelled to evaluate the initial pithing moment. This induced pitching moment just after the separation is found to be the root cause of the turn-over rotation. Since the translational velocity of the capsule is small just after the separation, it is resulting in the smaller aerodynamic restoring moment due to the small dynamic pressure. When the aerodynamic restoring moment is small, even smaller pitching moment can be result in the turn-over rotation. However, the small parachute attached to the sling cannot be removed because it is used to control the sling not to be entangled with the main parachute system. Therefore, the probabilistic trajectory analysis with including the side-wind effect is conducted to quantify the side wind criterion to prevent the initial turn-over. One of the typical results for the side wind velocity 15 m/s and 17.5 m/s are shown in Figure 25. The initial turn-over rotation is not occurred in the case that side wind magnitude is 15.0 m/s. While, the initial turn-over rotation is occurred in the case that it is 17.5 m/s. Based on these results, the side-wind criterion is set for the decision metrics to trigger the capsule separation.

Consequently, the smooth translational acceleration without turn-over rotation has been achieved by meeting the side wind criterion. Snapshot images viewing from the helicopter are shown in Figure 26. As a result, 4th High-altitude drop test has been fully success which was the important schedule milestone to meet the tight schedule to realise the HTV-7 mission.

Figure 24: High-altitude drop test configuration and cause of the turn-over rotation just after the separation.

Table 11: Flow conditions for high-altitude drop test analysis.

Mach number M_∞	0.15
Reynolds number Re_∞	1.225×10^6
Altitude $[km]$	1.920
Velocity U_∞ $[m/s]$	49.94
Pitch angle $[deg]$	$0 - 180$

Keiichiro FUJIMOTO, Takayuki ITOH, Hideyo NEGISHI, Ryoh NAKAMURA, Yasuhide WATANABE, Kota TANABE
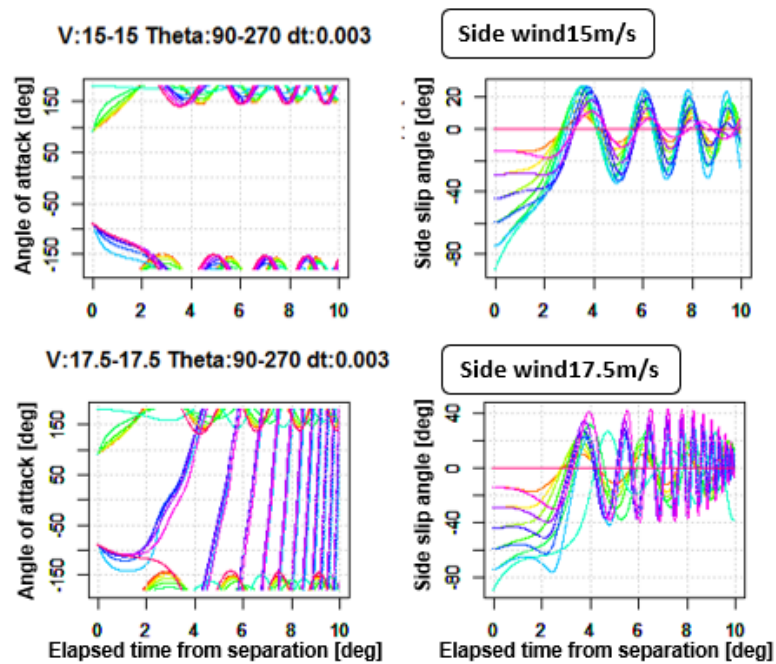
Figure 25: Side wind effects on the capsule's pitching motion.
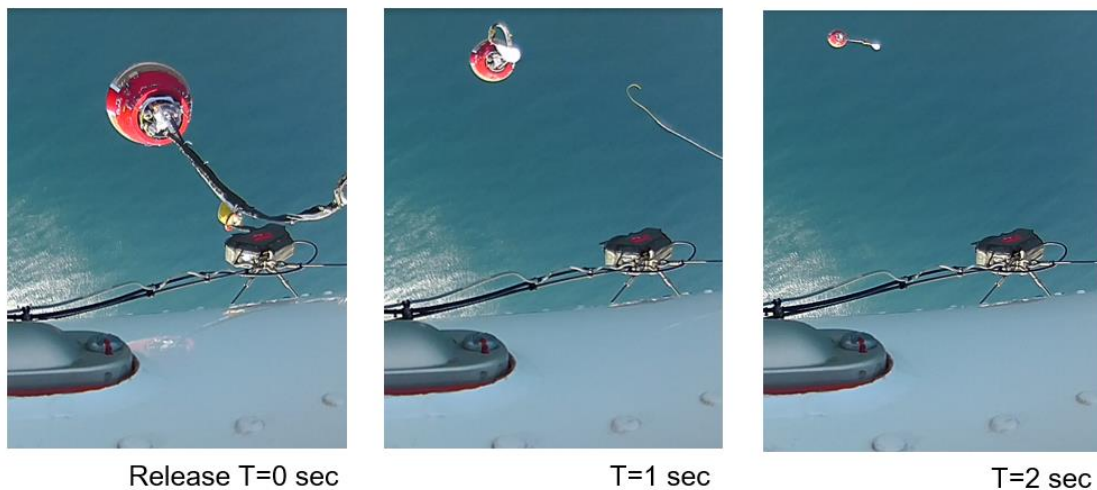
Figure 26: Smooth separation without turn-over spinning at 4th high-altitude drop test on 16/11/2017.

6. Conclusion

Successful result of HTV small re-entry capsule (HSRC) project was presented. Computational aerothermodynamic analysis methods and its contributions to the HSRC's design were overviewed and discussed. Local heat flux peak and the pressure increase are generated due to the hot gas main stream collision onto the wall near the RCS nozzle exit. Augmentation factor is roughly from 2.0 to 8.0, which is increased by the larger mass flow rate of the free-stream. Effect on the aerodynamic force and moment is significant, which is at least 5 times larger as comparing with the RCS thrust. Severe ablator erosion was not found and the precise GNC was achieved. TPS shell collision risk was identified and the shell release air-bag was employed. Its importance on the reliable parachute deployment is confirmed by the post-flight analysis. Conventional MILES-type CFD analysis is quantitatively accurate even for the unsteady flows such as the aeroacoustics characteristics prediction. Pressure fluctuation is induced by the unsteady shear layer whose frequency changes with the flow structures such as the local shock on the shear layer. Input sound pressure level is decided based CFD. 6DoF trajectory analysis was carried out to evaluate the side-wind criterion to prevent the turn-over rotation at the low dynamic pressure phase just after the separation. Drop test was succeeded by meeting the side-wind criterion.

References

[1] Shirouzu, M., Kai, T., Akimoto, T. and Shimoda, Y., "HYFLEX Project for the Development of HOPE," 19th International Symposium on Space Technology and Science, ISTS 94-g-12, May 1994.

[2] Inatani, Y., Ishii, N., Yamada, T., Hiraki, K., Yamada, K., Suzuki, T., and Fujita, K., "Post-flight analysis of Hayabusa; asteroid sample return capsule," Advances in the Astronautical Sciences, Vol. 146, pp. 685-696, 2013.

[3] Suzuki, Y., Imada, T., "Concept and Technology of HTV-R: An Advanced Type of H-II Transfer Vehicle," 28th International Symposium on Space Technology and Science, ISTS 2011-g-09, 2011.

[4] Fujimoto, K. and Nanbu, T., et al, "Validation of LS-FLOW for Reentry Capsule Unsteady Aerodynamic Analysis," AIAA Paper 2017-1411, 2017.

[5] Fujimoto, K., Negishi, H. and Nakamura, R., Nakakita, K., "Aero-Acoustics CFD Prediction for Re-entry Capsule Wake Flows at Subsonic to Supersonic Regine," AIAA Paper 2018-0520,2018 AIAA Aerospace Sciences Meeting, 2018.

[6] Haruki, M., Nakamura, R., Matsumoto, S., Kobayashi, S., Kawashima, I., Aoki, K., Kikuchi, N., "Post-Flight Evaluation of the Guidance and Control for Re-entry Capsule "HSRC"", 8th EUCASS, 2019.

[7] Fujii, K., Nakano, E., Mitsuo, K., Nagai, S., Tanno, H., Iemura, K., Takama, Y., Nakakita, K., Matsuyama, S., Fujita, K., Murakami, K., "Estimation of Aero- and Aerothermo-Dynamic Characteristics for HTV-R," The Journal of Space Technology and Science, Vol. 27, 2, pp. 31-43, 2014.

[8] Koga, S., Hidaka, A., Tagai, R., Kimura, T., Yoshinaga, T., Nagai, S., Nishijima, H., "Dynamic Stability Testing of a Reentry Lifting Capsule in a Transonic Wind Tunnel," AIAA 2014-1119, 2014.

[9] Tanno, H., Komuro, T., Itoh, K., "Free-Flight Test of HTV-R Capsule in Transonic Ballistic Range," The Journal of Space Technology and Science, Vol. 27, No.2, 2013.

[10] Takii, K., Kanazaki, M., Ishiko, K., Hayashi, K., Hashimoto, A., and Aoyama, T. "Unsteady Numerical Simulations of HTV-R Reentry Capsule by Using Detached-Eddy Simulation," 52nd Aerospace Sciences Meeting, AIAA SciTech Forum, AIAA paper 2014-0249, 2014.

[11] Hashimoto, A., Murakami, K., Aoyama, T., Tagai, R., Koga, S., Nagai, S. and Hayashi, K., "Dynamic Stability Analysis of a Reentry Lifting Capsule with Detached Eddy Simulation," 54th AIAA Aerospace Sciences Meeting, AIAA Paper 2016-0552, 2016.

[12] Tsutsui, Y., Takizawa, K., Toh, N., Boswell, C., Kolesar, R., Tezduyar, T. E., "FSI Analysis of JAXA HTV-R Parachute," 8E-5, pp. 426 – 427, 1st International Conference on Computational Engineering and Science for Safety and Environmental Problems (COMPSAFE2014), 2014.

[13] Fujimoto, K., "Study on the Automated CFD Analysis Tools for Conceptual Design of Space Transportation Vehicles," Ph.D. Dissertation, Univ. of Tokyo, Tokyo, Japan, 2006.

[14] Kitamura, K., Nonaka, S., Kuzuu, K., Aono, J., Fujimoto, K., and Shima, E., "Numerical and Experimental Investigations of Epsilon Launch Vehicle Aerodynamics at Mach 1.5," Journal of Spacecraft and Rockets, Vol.50, No.4, pp.896-916, 2013.

[15] Kitamura, K., Fujimoto, K., Shima, E., Kuzuu, K., and Wang, Z. J., "Validation of Arbitrary Unstructured CFD Code for Aerodynamic Analyses," Transactions of the Japan Society for Aeronautical and Space Sciences, Vol. 53, No. 182, pp. 311–319, 2011.

[16] Fujimoto, K., Fujii, K., and Wang, Z. J., "Improvements in the Reliability and Efficiency of Body-Fitted Cartesian Grid Method," AIAA Paper 2009-1173, 2009.

[17] Matsuyama, S., Takayanagi, H. and Fujita, K., "Numerical Investigation on RCS Jet Interactions for a Mars Entry Vehicle," AIAA Paper 2013-2977, 43rd AIAA Fluid Dynamics Conference, 2013.

[18] Chul Park, "Assessment of a two-temperature kinetic model for dissociating and weakly ionizing nitrogen," AIAA Journal of Thermophysics, Vol. 2, No. 1, 1988, pp. 8-16.

[19] V. L. Landau and E. Teller, "Zur Theorie der Schalldispersion", Physikalische Zeitschrift der Sowjetunion, Vol.10 (1936), pp.34-43.

[20] M. Johonson F.C. Blottner and M. Ellis. Chemically reacting viscous flow program for multicomponent gas mixtures. Report SC-RR-70-754,Sandia Laboratories, Albuquerque, New Mexico,1971.

[21] Reid, R. C., Prausnitz, J. M. & Poling, B. E. 1987 The properties of gases and liquids, 4th edn. New-York: McGraw-Hill.

[22] Y. Wada and M.S. Liou. "A flux splitting scheme with high-resolution and robustness for discontinuities," AIAA Paper 94-0083, 1994. (20) .

[23] van Leer, B. (1979), "Towards the Ultimate Conservation Difference Scheme. V. A Second-Order Sequel to Godunov's Method", Journal of Computational Physics 32, 101-136.

[24] Eberhardt, S., and Imlay, S., "Diagonal Implicit Scheme for Computing Flows with Finite Pate Chemistry," Journal of Thermophysics and Heat Transfer, Vol. 6, No. 2, 1992, pp. 208– 216.

[25] Baldwin, B. S. and Lomax, H., " Thin Layer Approximation and Algebraic Model for Separated Turbulent Flows", AIAA Paper 78-257, 1978.

[26] Shima, E., Kitamura, K., and Fujimoto, K., "New Gradient Calculation Method for MUSCL Type CFD Schemes in Arbitrary Polyhedra," AIAA   Paper 2010-1081, 2010.

[27] Mavriplis, D. J., "Revisiting the Least-Squares Procedure for Gradient Reconstruction on Unstructured Meshes," AIAA Paper 2003-3986,2003.

[28] Venkatakrishnan, V., "Convergence to Steady State Solutions of the Euler Equations on Unstructured Grids with Limiters," Journal of Computational Physics, Vol. 118, No. 1, 1995, pp. 120–130.

[29] Shima, E. and Kitamura, K., "On New Simple Low-Dissipation Scheme of AUSM-Family for All Speeds," AIAA paper 2009-136, 2009.

[30] Jameson, A., and Turkel, E., "Implicit Schemes and LU Decompositions," Mathematics of Computation, Vol. 37, No. 156, 1981, pp. 385–397.

[31] Baurle, A. R. and Tam, J. C., "Hybrid Simulation Approach for Cavity Flows: Blending, Algorithm, and Boundary Treatment Issues," AIAA Journal, Vol. 41, No. 8, August 2003, pp. 1463-1480.

[32] Andrew J. Hyatt and Molly White, "Orion MPCV Continuum RCS Heating Augmentation Model Development", 52nd Aerospace Sciences Meeting, AIAA SciTech, AIAA 2014-0511, 2014.

[33] Kawai, S. and Fujii, K., "Time-Series and Time-Averaged Characteristics of Subsonic to Supersonic Base Flows," AIAA Journal Vol.45, No.1, pp289-301, 2007.